amcs

A CUSTOM DEEP LEARNING ARCHITECTURE WITH IMAGE AUGMENTATION FOR INTELLIGENT GASTROINTESTINAL TRACT TISSUE CLASSIFICATION

MICHAŁ WIECZOREK [a,*], NATALIA WOJTAS [b], ROMAN WITUŁA [a],
ALEKSANDRA KRAWCZYK [c], KAROL RYCERZ [c]

[a]Faculty of Applied Mathematics
Silesian University of Technology
Kaszubska 23, 44-100 Gliwice, Poland
e-mail: michal.wieczorek@polsl.pl

[b]*PhD student*
University of Life Sciences in Lublin
Akademicka 12, 20-950 Lublin, Poland

[c]Department of Animal Anatomy and Histology
University of Life Sciences in Lublin
Akademicka 12, 20-950 Lublin, Poland

The origin of sampled tissue and characteristics of healthy organs is important for potential abnormality detection in veterinary medicine. Most often such information is given during the sampling process, but in some cases there is a possibility of mislabeling, especially in the education sector where some microscopic preparations might be made by students without proper knowledge or the inspected tissues are not of fully known origin. Occasionally, it is possible to determine the affiliation by searching characteristics of the organ in a sample; however, this is not always possible even for a skilled professional as some tissues vary too little between their counterparts in different species or even in different organs of the same species. Because of this, an automatic system able to perform such classification in a fraction of a second and with high accuracy can be helpful in such cases, especially considering the low cost of adding that solution to the current workflow. This paper presents a new dataset for healthy organ classification based on light microscope imagery containing 25 abstract classes of different organs of a few species. During the sampling process, 3680 images of healthy tissues were collected. Additionally, a custom deep learning architecture was created that is able to classify those samples between organs and species with a validation accuracy reaching 98.34%. Such performance is in some cases higher than that of a human specialist, especially when some examples have very small visual differences between one another or the classification is made on previously non-determining regions of the organ. Additionally, the collection of such a dataset provides a great opportunity for further work containing abnormality detection as it already provides information on the healthy organ description, which can be used for a deep learning model searching for illnesses or mutations. What is more, such a dataset and the corresponding artificial neural network constitute one of the first solutions of this kind in veterinary medicine, as most state-of-the-art papers focus on human medicine.

Keywords: deep learning, artificial intelligence, image augmentation, tissue classification, veterinary medicine.

1. Introduction

Proper classification of the origin of the examined tissue can be an essential decision factor about the performed diagnostics and later treatment. In human medicine it is less of an issue since all operations are performed on a single species, which allows for more specialized knowledge and less possibility for a mistake; however, in veterinary medicine, the multitude of different species and high variety of determining characteristics create an issue in such classifications. It is thus impossible for a single

---

*Corresponding author

human specialist from the field to have exact knowledge about the differences between all the labeling species, which requires more focus on proper sample labeling during the sampling phase. Due to the high amount of patients, varying standards governing such operations and the possibility of doctor fatigue there is a potential for a mistake during that process. Currently, such an issue is very difficult to spot manually and the diagnosis may be made based on wrong data, which can mislead the specialist into incorrect reasoning and later to the erroneous treatment of the patient. To overcome this issue many scientists are working on some automated solutions that may help with an early classification to help find mislabeled samples and give an alert to the specialist.

Most works however are done only on human patients and focus only on a few organs with the main point of finding specific anomalies. Such an example can be found in the work of Zhang *et al.* (2018). The paper addresses the problem of segmenting different types of liver tissue (parenchyma, viable tumor, and necrosis) on multi-parameter MR images in patients with hepatocellular carcinoma (HCC), a common and deadly form of liver cancer. The authors propose a patch-based learning scheme that uses a multi-resolution input, an auto-context design, and a multi-phase training procedure to improve the performance and efficiency of the segmentation task. Later they evaluate the proposed solution on a dataset of 20 patients and compare it with other CNN-based methods and a benchmark method that uses manually designed features and random forest classifiers. The paper shows that the proposed method achieves better results in terms of detection and delineation metrics, especially for medium and large-size anomalies.

Another interesting solution is given by Ker *et al.* (2019). The authors propose an automated process to classify histology slides of brain and breast tissues using the Google Inception V3 convolutional neural network (CNN). They report the benefit of transfer learning across different tissue types, such as brain and breast, to improve CNN accuracy for rare tumors with limited training data. For validation of their solution, the authors compare the CNN performance with human pathologists and other existing methods and use various metrics such as recall, precision, F1 score, and activation maps to evaluate the CNN performance. The ensembled networks achieved an accuracy of 96% in classifying grade 4 tumors, and an accuracy of 71% when classifying grade 2 and 3 tumors. The authors suggest that their proposed method can assist human pathologists in the triage and inspection of histology slides to expedite medical care, and can also improve CNN performance in cases where the training data is limited.

Zahia *et al.* (2018) propose a novel method for automatic tissue segmentation in pressure injuries

based on a convolutional neural network (CNN). Their proposed method classifies different tissue types (necrotic, granulation and slough) by learning their features from small image patches. The authors evaluate their method using various metrics and achieve an overall average classification accuracy of 92.01% and an average total weighted Dice similarity coefficient of 91.38%. They also obtained an average precision per class of 97.31% for granulation tissue, 96.59% for necrotic tissue, and 77.90% for slough tissue. The authors claim that the presented method can handle complex structures in the images and provide a robust solution for pressure injury assessment.

Khorshed *et al.* (2020) present a novel deep-learning framework for multi-tissue cancer classification based on whole-transcriptome gene expressions. They designed a new convolutional neural network architecture called GeneXNet, which is specifically tailored to handle gene expression data. GeneXNet can learn genomic signatures that are relevant for cancer diagnosis across multiple tissue types without requiring any prior gene feature selection. GeneXNet can also detect genetic alterations that drive cancer progression and provide biological insights through visualization techniques. The authors evaluate GeneXNet on a large dataset of human samples representing 33 different cancer tumour types across 26 organ sites. They report that GeneXNet achieves an impressive classification accuracy of 98.9%. They also demonstrate how GeneXNet can be used for transfer learning to build classifiers for tumors that have insufficient samples to train independently.

Wojtas *et al.* (2023) created a custom semantic-segmentation convolutional deep neural network architecture for malaria detection in veterinary medicine based on imagery from a light microscope. The proposed solution allowed for an exact masking application, which classified the elements into healthy blood cells, malaria-infected cells and background with a very high classification accuracy of over 99%. The custom architecture was also made with a lightweight computation in mind making it a helpful addition for the potential clinic, where it would not require huge computing power to be able to properly function. Rak *et al.* (2023) presented an interesting hybrid classifier to predict an artery disease with a high precision. Their use of aggregating base classifiers combined with applying the distributivity equation, resulted in better classification accuracy and overall performance.

As can be seen, most of the papers from other authors focus only on humans and specific illnesses, while the approach presented in our paper focuses on a variety of animals and a more global selection of abstract classes.

Another important factor is image augmentation. It is a technique of artificial generation of surrogate data in order to enlarge the training dataset to improve the validation accuracy. Some of the techniques include

simple image transformations like random image rotation, flips, crops or changing colours. However, some authors have created more advanced solutions.

Such an example can be found in the work of Oza *et al.* (2022). The article covers basic and advanced augmentation techniques with a focus on medical imagery, such as geometric transformations, noise injection, kernel filters, GANs, and others. One of the interesting examples is pixel-level augmentation, which is helpful for research in medical imaging fields, as such images are obtained with different technologies and imaging modalities and because of that they can be essentially assorted in pixel intensities. In pixel-level augmentation, intensities of pixels are perturbed with random noise and a given probability, also called intensity variation. Additionally, a pixel-level augmentation modifies the brightness of an image, e.g., by using gamma correction, image blurring, and image sharpening.

Another example is given by Abayomi-Alli *et al.* (2020). Here the authors propose a novel image augmentation technique based on a random permutation of coefficients of within-class principal components obtained after applying principal component analysis (PCA). In such a way, after a short pre-training the augmentation network learns some differences in images from the training dataset and later generates new images based on that knowledge. Later those images are included in the final training dataset, which helps improve the validation accuracy.

Optimizing the deep learning model for a specific task is an important addition to a well-designed model architecture. One of such examples can be found in the work of Karlupia *et al.* (2023). They employed a genetic-algorithm-based optimization for convolutional neural networks for face recognition. As it is one of the most active fields of computer vision, creation of a novel approach with better performance than before is a difficult task and requires a high amount of creativity and knowledge. In the presented paper, the focus was on creating a genetic-based fine-tuning of CNN hyper-parameters such as the filter size or the numbers of filters and hidden layers. In such a way, during the training and optimization processes, the network is dynamically modified to create a near-perfect architecture that is both lightweight and has high accuracy. The authors also performed a series of experiments comparing their solution with existing CNN models and achieved a higher detection accuracy of 94.5% with a relatively small addition of time needed to train the final model.

Another interesting mathematical model for training optimization has been made by Yang *et al.* (2023). In this paper, a novel algorithm for improving the detection of small elements on complex backgrounds called the local gradient contrast method (LGCM) has been proposed. As in many datasets, the main object is small and the rest of the image can be cluttered. This creates a problem of a low signal-to-noise ratio, which drastically reduces the ability of classical CNN models to robustly detect targets submerged in such noisy images. The authors present a novel method that firstly obtains the optimal scale for each pixel by calculating a multiscale salient map, then a subblock-based local gradient measure is designed, which can suppress strong clutter interference and pixel-sized noise at the same time. Finally, such computed data are utilized to construct the LGCM, which creates an adaptive threshold that allows for better feature extraction of small elements. To test this model the authors performed a series of experiments which proved that their method yields superior results in comparison with other state-of-the-art methods.

In this paper, we present a novel, lightweight convolutional neural network architecture for organ classification of many species based on tissue images from a light microscope. All computations have been made on a custom-made image dataset containing 25 classes of abstraction combined with a custom augmentation pipeline. Such a combination allowed for a very high validation accuracy.

2. New custom dataset

2.1. Importance of custom data. A good quality and valid dataset is a necessary factor of the desired model's creation. Without specific data about the subject of interest, designing and training of a machine learning model is impossible, especially in fields like medical data processing. In this paper we present a custom deep learning architecture for gastrointestinal tract tissue classification for animals, which due to its novelty had no open access datasets found during the research phase; this leads to a decision to create a custom one suited for this task. The so prepared dataset has also lots of advantages over a generic dataset such as having more control over the quality and quantity of data, having all needed labels, etc.

2.2. Overview. Due to the lack of a suitable dataset for our problem, in the presented work, we have collected our own dataset. This dataset contains 3680 light microscope images distributed to over 25 abstract classes. Examples of such images can be found in Fig. 3. As can be seen, there is a high variety of photographed tissues that are scattered in different organs belonging to different animal species. For the use in this paper, we have selected 25 classes containing around 100 images per class. Some classes from the collected dataset have been removed due to the fact that there were some classes with the same organ just with different coloring, which was unnecessary for this research.

The classes in the data collection are the following:

1. Reticulum (c),
2. Stomach—fundus (p),
3. Duodenum (h),
4. Duodenum (p),
5. Ileum—lymphatic nodules (p),
6. Jejunum (h),
7. Caecum (p),
8. Omasum (c),
9. Stomach—pylorus,
10. Colon (h),
11. Colon (p),
12. Oesophagus (p),
13. Sublingual salivary gland (c),
14. Sublingual salivary gland (p),
15. Submandibular salivary gland (h),
16. Submandibular salivary gland (c),
17. Parotid salivary gland (c),
18. Abomasum (c),
19. Pancreas (c),
20. Liver (h),
21. Liver (p),
22. Proventriculus (b),
23. Gizzard (b),
24. Stomach—cardia (p),
25. Rumen (c),

where

- p: pig,
- h: horse,
- c: cow,
- b: bird.

2.3. Data collection process and methodology. The histological specimens utilized in this study were sourced from the slide collections of the Department of Histology and Embryology at the University of Life Sciences in Lublin. These tissue samples were derived from various animal species, including cows, horses, pigs, and birds. The slides were prepared over a span of several years and have been preserved as demonstration specimens for veterinary medicine classes. Each specimen was fixed in 10% formalin, dehydrated in increasing concentrations of alcohol solution, cleared in xylene, infiltrated with paraffin, and embedded in paraffin blocks. Subsequently, these blocks were sectioned into 10-micrometer slices using a microtome, and these sections were placed on glass slides. The slides were stained using the hematoxylin and eosin (H+E) technique. Prior to the application of the dyes, the slides were rehydrated in a graded series of alcohol. The slides were then incubated in hematoxylin (Chempur, Piekary Ślaskie, Poland) for 5 minutes, rinsed in running water, and eosin (Chempur, Piekary Ślaskie, Poland) was applied for 3 minutes. Post-staining, sections were rehydrated, cleared in xylene, and mounted in DPX (Sigma-Aldrich, St. Louise, USA). The microphotographs utilized in this study were captured under a Leica DM500 light microscope equipped with a Leica ICC50W camera and a $10\times$ magnification lens.

For a better deep learning model creation as a proof of concept, images were taken not only of the characteristic regions but also of the regions non-determining for human. In such a way, there was a possibility to check if the neural network can differentiate organs in a different way.

All photographed organs are described in more detail in what follows. The data collection scheme is presented in Fig. 1 and the abstract classes with example images are shown in Fig. 2.

The digestive system in animals demonstrates a specific histological structure that is precisely adapted to their specific dietary requirements. The following is a detailed description of individual systems and organs, highlighting the species-specific differences therein.

2.4. Salivary glands. Salivary glands are compound acinar (parotid gland), tubuloacinar (sublingual gland) and acinotubular (submandibular gland) glands. The parenchyma forms the glandular portions of each gland, while the supporting connective tissue is referred to as the stroma (Carubbi *et al.*, 2018).

All salivary glands have a lobular structure and are surrounded by a connective tissue capsule. The salivaries histologically are differentiated from one another on the basis of the parenchyma structure containing different secretory units with intralobular ducts. Within the intralobular ducts, intercalated ducts with simple cuboidal epithelium and striated ducts lined with simple cylindrical epithelium are distinguished. The glandular portions of the salivary glands may be mucous (tubular, with irregular lumen, lined with simple cuboidal epithelium which constitute cells filled with mucous—poor staining) or serous (acinar with small lumen, lined with simple cuboidal epithelium in which cells are filled with zymogen granules—intensive red staining) or mixed (tubular with serous demilunes) (Bodes and Martínez, 2023; Porcheri and Mitsiadis, 2019; Bacha Jr and Bacha, 2012).

2.5. Digestive tract. The digestive tract, starting from the oesophagus and ending with the anus, is tubular and contains four layers of the histological structure which are as follows:
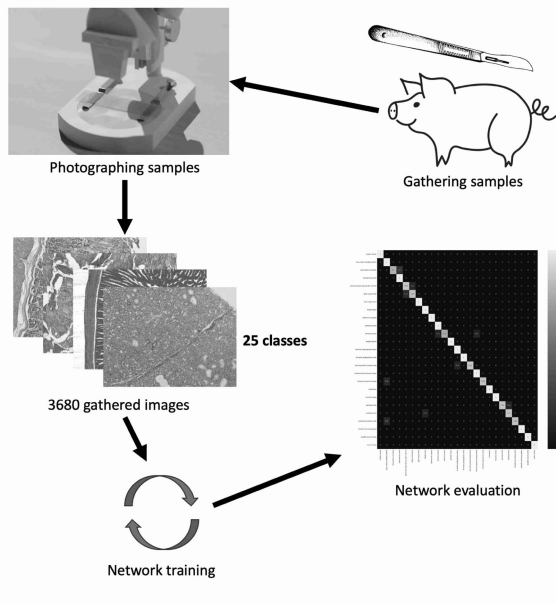
(i) the mucous membrane (tunica mucosa), which

Fig. 1. Dataset creation and evaluation scheme.

Fig. 2. Defined dataset classes shown with example images.

includes an epithelial lining that may occur in various forms as stratified squamous epithelium or simple columnar epithelium, a supporting lamina propria and the lamina muscularis;

(ii) the submucous membrane (tunica submucosa) being a connective tissue layer which may contain lymphatic follicles, nerve plexi, and submucosal glands;

(iii) the muscular membrane (tunica muscularis) which may contain both smooth muscle tissue and striated skeletal muscle tissue; in most parts of the digestive tract it is formed by two layers of muscles: internal circular and external longitudinal;

(iv) the adventitia in extraperitoneal parts of the tract and serous membrane (tunica serosa) within the peritoneal cavity,

(cf. Markovits *et al.*, 2013; Mahadevan, 2020; Bodes and Martínez, 2023).

2.6. Oesophagus. The oesophagus is a tubular organ characterized by its four-layered structure. Microscopic identification of the oesophagus across different species requires extensive practice due to the existence of subtle differences.

The mucosa is covered with stratified squamous epithelium which may become keratinized in herbivores. The lamina propria, composed of loose connective tissue, forms numerous papillae, especially high in cattle. Single lymphatic follicles may be present, in particular in pigs (Bazira, 2023). The lamina muscularis is composed of smooth muscle cells that run longitudinally or obliquely. In horses, ruminants and carnivores, this layer consists of individual bundles of muscle cells that connect with each other near the stomach to form a continuous layer. In dogs and pigs, it may be observed only in the caudal part of the oesophagus (Jones *et al.*, 2022; Voutsinou *et al.*, 2018).

The submucosa consists of loose connective tissue in which the oesophageal glands can be found. In dogs they are present throughout the entire length of the organ; in pigs, they are abundant in cranial part; in horses, cats and ruminants they can be found only at the pharyngoesophageal junction. The tunica muscularis consists of an inner circular layer and an outer longitudinal layer (Botlagunta and Kedari, 2023). In the rabbits, carnivores, birds, horses and ruminants, the number of layers may be higher—from three to even four layers (pig). In pigs, there are skeletal muscles in one-third of the oesophagus, mixed muscles in the middle third and smooth muscles in the caudal third. In horses, two thirds of the organ contain skeletal muscles and in cats they may extend up to four-fifths of the oesophagus length (Shiina *et al.*, 2005; Kuryszko *et al.*, 2019). In ruminants and dogs, only striated skeletal muscles appear along the entire length. The adventitia surrounds the oesophagus in its cervical part, turning into a serous membrane in the thoracic part (Watson, 1973; Dawood *et al.*, 2022; Shiina *et al.*, 2005; Jones *et al.*, 2022).
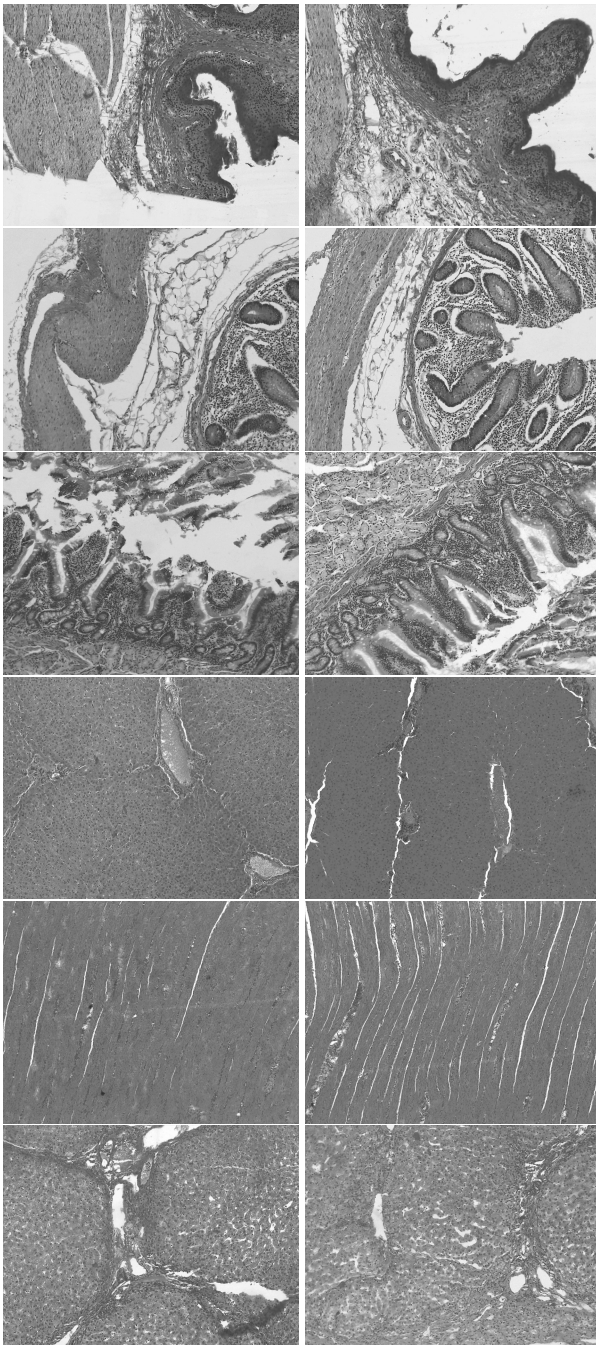
Fig. 3. Different examples of collected images. In the first row we can see the cow reticulum, in the second row a pig's caecum is presented, the third row belongs to a pig's duodenum, the fourth row is a horse liver, the fifth row is a bird gizzard and the sixth row is a pig's liver. Some color shifts are present due to the nature of microscope imaging and some contamination in photographed samples.

2.7. Stomach. The anatomical structure of the stomach exhibits considerable variations in structure across different animal species, which is primarily due to the specific nutritional requirements of each species. In carnivores the stomach lining is composed of a glandular mucosa. Herbivorous species feature an additional nonglandular region which is particularly well-developed in ruminants. It constitutes the lining of all forestomachs. Upon histological examination, the glandular region of the stomach can be further classified into three distinct areas: the cardiac, the fundic and the pyloric gland region (Suganuma *et al.*, 1981; Zahariev *et al.*, 2010).

The mucosa of the glandular region is lined with simple cylindrical epithelium. Underneath, there is a lamina propria composed of loose connective tissue, with lymphatic follicles and gastric glands (Doyama *et al.*, 2021). The lamina muscularis comprises smooth muscle cells concentrated in two layers: an inner circular and an outer longitudinal layer. In carnivorous animals, a subglandular layer made of regular dense connective tissue is present. The mucous membrane forms gastric folds, which increase the surface area of the stomach and, by stretching, allow its volume to expand when filled with food (Bazira, 2023; Hogben *et al.*, 1974).

The submucosa is composed of loose connective tissue with numerous collagen fibres. The tunica muscularis comprises three layers of smooth muscle cells: an inner oblique layer, a middle circular layer, and an external longitudinal layer. The serous membrane is composed of a mesothelium lying on the loose connective tissue (Hogben *et al.*, 1974; Zahariev *et al.*, 2010).

The non-glandular region of the mucosa, within the single-chambered stomach, is present in horses and pigs. It is lined with stratified squamous epithelium which may be keratinized to varying degrees. In ruminants the nonglandular portion extends to form forestomachs: rumen, reticulum and omasum (Hewetson and Tallon, 2021). Their histological structure is similar due to the presence of mucosa lined with stratified squamous epithelium, submucosa with connective tissue stroma, two-layered tunica muscularis with smooth muscles and serosa covered with mesothelium (Kararli, 1995; Amorim *et al.*, 2016; Friedland *et al.*, 1971; Ghoshal and Bal, 1989).

The ruminal mucosa and submucosa form a small tongue-shaped papillae. There is no lamina muscularis and the lamina propria merge with submucosa forming propria-submucosa protruding into the ruminal papillae. The reticulum has a similar structure with propria-submucosa covered with stratified squamous epithelium. These layers form a reticular papillae with muscularis mucosa located only in the upper part of the papillae. The omasum is characterized by a long omasal laminae formed of mucosa, submucosa and tunica muscularis which sends parts of muscles from a circular

layer to the laminae. The lamina muscularis is present and forms a thick layer beneath the lamina propria. Lamina muscularis and tunica muscularis merge at the top of large laminae forming a muscular marginal shaft (Lechner-Doll *et al.*, 1995; Stieger-Vanegas and McKenzie, 2021; Sellers and Stevens, 1966; Chungath, 1981; Markovits *et al.*, 2013).

The avian stomach contains a proventriculus and a gizzard. The proventriculus is lined with a simple columnar epithelium that protrudes into the lamina propria of the mucosa, forming surface tubular glands. Within the submucosa, there are proper glands arranged in glandular buds. The tunica muscularis contain inner and outer longitudinal layers and a middle circular layers of smooth muscles. Serosa contains mesothelium and connective tissue (Hristov, 2020).

The gizzard comprises thick tunica muscularis with smooth muscles arranged in an alternating circular and longitudinal pattern, enveloped by a layer of tendon sheath that refers to the submucosa. The luminal side is characterized by a mucous membrane covered with simple cuboidal epithelium which forms tubular glands protruding to lamina propria. The secretion from these glands forms a gastric cuticule (Kuryszko *et al.*, 2019; Catroxo *et al.*, 1997; Al-Juboory *et al.*, 2017; Taki-El-Deen, 2017).

2.8. Intestines. The intestine, an integral component of the digestive system, exhibits a unique histological structure tailored to its specific role in digestion. It is divided into two main sections: the small intestine and the large intestine. The small intestine is further subdivided into the duodenum, jejunum, and ileum, while the large intestine comprises the colon, cecum, and rectum (Bodes and Martínez, 2023; Lingeman and Garner, 1972).

The mucosa of the intestines typically comprises a simple columnar epithelium, lamina propria and lamina muscularis. These layers form finger-like projections called villi. The villus contains a connective tissue core with blood vessels, lymphatic capillary-lacteal in the center and longitudinally oriented smooth muscle cells. The length and thickness of the intestinal villi vary across species, with dogs having the longest and thinnest villi, ruminants having short and thin villi, and horses and pigs exhibiting intermediate forms. Within the lamina propria, there are simple tubular intestinal glands. In this layer, single lymphatic follicles can be found (Chivers and Hladik, 1980; McQuilken, 2021).

The epithelium of the mucosa contains enterocytes, characterized by a presence of microvilli demonstrated as a brush border under the light microscope. There are also numerous goblet cells within the epithelium (Jones *et al.*, 2022; Hostetter and Uzal, 2022).

The submucosa is composed of loose connective tissue. It may also contain single lymphatic follicles.

When speaking about the duodenum, duodenal glands can be also found specific only to this section, which are of the intestine and in the case of ileum-aggregated lymphatic follicles that descend there from the mucous membrane.

The tunica muscularis contains inner circular and outer longitudinal layers of smooth muscles, while the serous membrane covers the entire small intestine, except for the extraperitoneal section of the duodenum which is lined with adventitia

The structure of the large intestine is strictly adapted to the function it performs. The structure of its layers is similar to that of the small intestine, albeit with several distinguishing features. In the large intestines, there are no villi and the mucosal surface is smooth (Angelou *et al.*, 2023; Badawi *et al.*, 1998).

The mucous membrane is lined with a simple columnar epithelium and contains a thick lamina propria with a large number of intestinal glands in goblet cells. The glands formed by an invaginated mucosa may disrupt the lamina muscularis and extend to the submucosa.

The structure of the tunica muscularis is similar to that in small intestines. Additionally, in horses and pigs, the outer longitudinal layer in the cecum and colon forms large and flat muscle bands with elastic fibres, the taenia ceci and taenia coli.

In the final section of the rectum the intestinal crypts disappear and the simple stratified columnar epithelium is replaced by a stratified squamous epithelium which keratinizes in the anus. The lamina propria of the mucous membrane houses lymphatic tissue, lymphatic follicles and anal glands (Sheahan and Jervis, 1976; Kotzé *et al.*, 2010).

2.9. Liver. The liver is covered by the peritoneum beneath which a fibrous capsule is located. Connective tissue strands extend into the liver dividing it into liver lobules. The amount of interlobular connective tissue is minimal in horses, ruminants, carnivores, rodents, and certain birds, while it is abundant in pigs, camels, turkeys, ducks, and geese. In every animal species, there are expanded areas of interlobular connective tissue supporting branches of the hepatic artery, branches of the portal vein and a bile duct lined with simple cuboidal epithelium. These three structures form a liver triad in a portal area (Eberlova *et al.*, 2020).

Within the hepatic lobule, there are hepatocytes arranged in radial rows extending from the central vein. Between the bars of hepatocytes, there are sinusoid capillaries which lead the blood into the central vein. The hepatocytes surface form a bile canaliculi where the bile is secreted and transported to the bile ducts in the portal areas (Lidbury *et al.*, 2017; Banzato *et al.*, 2015).

2.10. Pancreas. The pancreas is a tubulo-acinar, lobulated gland with both exocrine and endocrine parts. It is encased in a serous membrane, beneath which there is a thin connective tissue capsule. From this capsule, strands of connective tissue penetrate the parenchyma, dividing it into lobules (Newman *et al.*, 2006).

The pancreatic parenchyma separated into distinct lobules comprises an exocrine part with a tubuloacinar secretory units with pyramidal cells and a small lumen. The tubular portion is more prominent in ruminants. The intercalated excretory ducts initiate directly within the glandular portions forming a centroacinar cells. The intralobular ducts are continued by interlobular ducts, pancreatic and accessory pancreatic ducts until they reach the duodenum (Longnecker and Thompson, 2023).

The endocrine part of the pancreas is composed of clusters of endrocrine cells, forming the pancreatic islets. Numerous sinusoid capillaries and a network of reticular fibres are present between these cells (Tsuchitani *et al.*, 2016).

2.11. State of the art of AI in histology. The subtle differences and intricate details distinguishing individual organs of the digestive system, as well as the challenges associated with species diversity, pose significant difficulties for laboratory personnel, novice doctors, students, scientific institutions, and learners. Identification of specific structures is often complicated by the inherent individual differences in living organisms, which may deviate from the idealized representations found in textbooks or articles. This discrepancy can lead to frustration and extended periods of uncertainty during the identification process. Furthermore, the described identification possibilities are often quite subjective, such as the assessment of whether intestinal villi are long and narrow or shorter and thicker. The physiology of living animals means that structures often exhibit characteristics that lie somewhere between the features typically assigned to a given organ or species. In such instances, individuals often reach an impasse, lacking additional tools to aid interpretation or resort to probabilistic judgments that carry a high risk of error. The artificial intelligence tool proposed in this article represents an initial attempt to develop a resource that can assist both novices grappling with interpretative dilemmas in the realm of histology and professionals seeking to expedite their workflow. Often, novices lack access to mentors who can answer troublesome questions, a common scenario in small diagnostic facilities. Professionals, on the other hand, can use this tool to significantly reduce their working time and cross-verify their results in case of doubt.

The current state of research on artificial intelligence (AI) in histology and histopathology is quite promising. AI methods have significantly enhanced our ability to extract quantitative information from digital histopathology images. These methods are expected to reduce the workload for human experts, improve the objectivity and consistency of pathology reports, and have a clinical impact by extracting hidden information from routinely available data

The field of histology and histopathology is witnessing promising advancements with the integration of AI. The available AI methodologies have substantially augmented our capacity to extract quantitative data from digital histopathology images. These methodologies are anticipated to alleviate the workload of human experts, enhance the objectivity and consistency of pathology reports, and make a clinical impact by extracting concealed information from routinely available data. In the realm of veterinary medicine, including histology, the application of AI is rapidly evolving. Most AI applications in veterinary medicine are predominantly academic, with a few commercial products as exceptions. Some commercially available products in veterinary medicine encompass automated analysis of x-ray radiographs (Basran, 2024). They are also focusing on employing radiomics-based research, and data-driven analysis of medical images, for a variety of companion animal cancers (Rakha *et al.*, 2021). Given the accelerating pace of this technology, it is expected that various forms of AI will be adopted in veterinary applications.

In conclusion, while AI holds substantial promise in the field of veterinary histopathology, challenges remain to be addressed (Ezanno *et al.*, 2021). First of all, there is a problem with the high price of such solutions, as the current technologies are provided to the users as physical devices with software hard-coded inside them. Such a solution is more profitable to creators as the user has no control over the equipment and has zero upgrade possibilities and it makes the price much higher. Also, it creates an accessibility problem because such devices need to be manufactured, sent and placed in a specialized room. Such devices are often very slow and have old hardware, which reduces the time and money benefit. Additionally, it requires changing human specialists' behavior in performing a diagnosis or classification as it adds more steps including use of the machine. The presented solution is purely software-based, so that it reduces the need for additional equipment, and allows the user to quickly add such a solution to the current pipeline. Also, if the hardware is too slow, it can be easily upgraded in the future without the need of buying the program again. All updates can also be done via the Internet, which is much faster and safer than upgrading the physical device. What is more, this paper focuses on lightweight AI, which can be quickly evaluated, and allows for more examinations at the same time.

3. Image augmentation and balancing

The custom dataset has been made with the focus on a balance of the abstract classes and included most of the photographed samples to allow the network to predict the tissue origin based on the majority of the visible structures. However, due to the time restrictions, the number of images per class was around 100 images. Such an amount is good to create a basic understanding of the characteristics differences but due, to a high amount of detected classes, it is not enough to ensure high validation accuracy. Because of that, this paper presents an augmentation algorithm that enriches the training dataset with modified samples, which then allows for better training and evaluation. The proposed image augmentation is presented as Algorithm 2, where img_1 is an input image, lab_1 is an input label, img_res is the processed image resolution and ψ is the number of repetitions. For our final network, ψ, has been set to 200 and img_res to 256×256. As the given images are from light-microscopy made on a white background, all the images have been inverted so the MaxPooling layers from the model architecture can properly detect important features instead of the background. During the research it was found that some basic transformations like horizontal and vertical flips, as well as random rotations help to deal with the low number of samples; however, to achieve the full accuracy, some color jitter transformations were needed to reduce the bias made by different lighting or coloring of the samples. Some more transformations changing the shape or generating new data should be avoided to reduce the error made by augmentation and allow the network to learn valid characteristics instead of the fake ones.

First, we need to define a bicubic interpolation

$$f(x, y) = \sum_{i=0}^{3} \sum_{j=0}^{3} a_{ij} x^i y^j. \tag{1}$$

Next we define an image resize algorithm,

$$resize(img_1, w, h) = \sum_{i=0}^{w-1} \sum_{j=0}^{h-1} \left(\sum_{k=0}^{3} \sum_{l=0}^{3} a_{kl} x^k y^l \right), \tag{2}$$

where img_1 is the original image, w and h are respectively the desired width and height, x and y are the normalized coordinates of the point in the original image, and a_{kl} are the coefficients that depend on the pixel values and derivatives at the four corners of the 4×4 grid. This equation applies the bicubic interpolation formula to each pixel of the resized image defined in (1).

Now we need to define an image rotation equation

$$\begin{bmatrix} x' \\ y' \end{bmatrix} \begin{bmatrix} \cos\theta & -\sin\theta \\ \sin\theta & \cos\theta \end{bmatrix} \begin{bmatrix} x \\ y \end{bmatrix}, \tag{3}$$

where (x, y) are the original coordinates of a point in the image, (x', y') are the rotated coordinates of the same point, and θ is the angle of rotation in radians. In order to convert the angle from degrees into radians, we can use the equation

$$\theta = \frac{\pi}{180} \times d, \tag{4}$$

where d is a desired degree. Now we can create a function to apply (3) and (4) on an image:

$$\begin{aligned} rotate&(img_1, d) \\ &= \begin{bmatrix} \cos(\frac{\pi}{180} \times d) & -\sin(\frac{\pi}{180} \times d) \\ \sin(\frac{\pi}{180} \times d) & \cos(\frac{\pi}{180} \times d) \end{bmatrix} \times \begin{bmatrix} x - x_0 \\ y - y_0 \end{bmatrix} \\ &+ \begin{bmatrix} x_0 \\ y_0 \end{bmatrix}, \end{aligned} \tag{5}$$

where (x_0, y_0) are the coordinates of the center of rotation, which are $(0, 0)$ in our case. This equation is based on the fact that to rotate an image around a point other than the origin, we need to first translate the image so that the center of rotation coincides with the origin, then apply the rotation matrix, and then translate the image back to its original position.

For most image color transformations, we have first to convert the RGB to the hue-saturation-lightness (HSL) representation:

$$\begin{aligned} &rgb\_hsl(img_1) \\ &= \begin{cases} R' = \frac{R}{255}, \\ G' = \frac{G}{255}, \\ B' = \frac{B}{255}, \\ M = \max(R', G', B'), \\ m = \min(R', G', B'), \\ C = M - m, \\ L = \frac{M+m}{2}, \\ S = \begin{cases} 0 & \text{if } C = 0, \\ \frac{C}{1 - |2L-1|} & \text{otherwise}, \end{cases} \\ H = \begin{cases} 0 & \text{if } C = 0 \\ 60° \times (\frac{G'-B'}{C} \bmod 6) & \text{if } M = R', \\ 60° \times (\frac{B'-R'}{C} + 2) & \text{if } M = G', \\ 60° \times (\frac{R'-G'}{C} + 4) & \text{if } M = B', \end{cases} \end{cases} \end{aligned} \tag{6}$$

where R is red, G is green, B is blue, M is the maximal value, m is the minimal value, C is chroma, L is luminance, S is saturation on H is hue.

To change saturation first, we have to define what the saturation is, i.e.,

$$S = \frac{\max(R, G, B) - \min(R, G, B)}{\max(R, G, B) + \min(R, G, B)}, \tag{7}$$

where S is the saturation, R is red channel, G is the green channel and B is the blue component of the image. This

formula is based on the HSL color model. Now, if we want to change the image saturation, we can multiply the S component by some multiplier x,

$$S' = x \times S. \tag{8}$$

Now, to get the final RGB values, we need to convert the image back from HSL to RGB:

$$hsl\_rgb(img_1)$$
$$= \begin{cases} R' = L + S'(L - 0.5)(1 - |2L - 1|), \\ G' = L + S'(L - 0.5)(1 - |2L - 1|), \\ B' = L + S'(L - 0.5)(1 - |2L - 1|), \end{cases} \tag{9}$$

where L is the lightness, and R', G', and B' are the new red, green, and blue components. The final saturation equation can be then defined as

$$change\_saturation(img_1, f)$$
$$= \begin{cases} img_2 = rgb\_hsl(img_1), \\ img_2.S = img_2.S \times f, \\ img_2 = hsl\_rgb(img_2). \end{cases} \tag{10}$$

To change the brightness we use a simple equation

$$change\_brightness(img_1, f)$$
$$= \begin{cases} R' = \min(\max(R \times f, 0), 255), \\ G' = \min(\max(G \times f, 0), 255), \\ B' = \min(\max(B \times f, 0), 255), \end{cases} \tag{11}$$

where R', G', B' are the new red, green, blue component values and f is a multiplier.

One possible way to change the contrast of a 2D image is to apply a linear transformation to the pixel values, such that the minimum and maximum values in the input image are mapped to the desired values in the output image. For example, if we want to map the input range $[a, b]$ to the output range $[c, d]$, we can use the following formula:

$$y = \frac{d - c}{b - a}(x - a) + c, \tag{12}$$

where x is the input pixel value and y is the output pixel value. This formula can be applied to each channel of an RGB image separately, or to a single channel of a grayscale or HSV image. This method is also known as contrast stretching or histogram stretching. A possible

equation for this method is

$$change\_contrast(img, f)$$
$$= \begin{cases} [a_R, b_R] = [\min(R), \max(R)], \\ [a_G, b_G] = [\min(G), \max(G)], \\ [a_B, b_B] = [\min(B), \max(B)], \\ [c_R, d_R] = [a_R, b_R] \times f, \\ [c_G, d_G] = [a_G, b_G] \times f, \\ [c_B, d_B] = [a_B, b_B] \times f, \\ R' = \frac{d_R - c_R}{b_R - a_R} \times (R - a_R) + c_R, \\ G' = \frac{d_G - c_G}{b_G - a_G} \times (G - a_G) + c_G, \\ B' = \frac{d_B - c_B}{b_B - a_B} \times (B - a_B) + c_B, \end{cases} \tag{13}$$

where R, G, and B are the original RGB values, R', G', and B' are the new RGB values, and $[a_R, b_R]$, $[a_G, b_G]$, and $[a_B, b_B]$ are the input ranges for each channel, and $[c_R, d_R]$, $[c_G, d_G]$, and $[c_B, d_B]$ are the output ranges for each channel.

The hue component is changed as

$$H' = (H + \theta) \mod 1, \tag{14}$$

where θ is a value by which the hue is shifted. Now the whole process of changing the hue of an RGB image is

$$change\_hue(img_1, f)$$
$$= \begin{cases} img_2 = rgb\_hsl(img_1), \\ img_2.H = (img_2.H + f) \mod 1, \\ img_2 = hsl\_rgb(img_2). \end{cases} \tag{15}$$

To flip a 2D image horizontally, we have to reverse the order of the pixels in each row of the image. This can be done by applying a transformation matrix to the coordinates of each pixel. The transformation matrix for horizontal flipping is

$$Hor = \begin{bmatrix} -1 & 0 & w \\ 0 & 1 & 0 \\ 0 & 0 & 1 \end{bmatrix}, \tag{16}$$

where w is the image width. This matrix will multiply each pixel coordinate (y) by -1 and then add w to the result, effectively moving the pixel to the opposite side of the image. The y coordinate will remain unchanged. For example, if the image has a width of 10 pixels and we want to flip the pixel at $(3, 4)$, we get

$$\begin{bmatrix} -1 & 0 & 10 \\ 0 & 1 & 0 \\ 0 & 0 & 1 \end{bmatrix} \begin{bmatrix} 3 \\ 4 \\ 1 \end{bmatrix} \begin{bmatrix} -3 + 10 \\ 4 + 0 \\ 1 + 0 \end{bmatrix} \begin{bmatrix} 7 \\ 4 \\ 1 \end{bmatrix}. \tag{17}$$

As a result, the pixel at $(3, 4)$ will be moved to $(7, 4)$. Thus, we can flip the entire image horizontally. Accordingly,

$$flip\_horizontal(img_1) = apply(img_1, Hor), \tag{18}$$

where

$$apply(img_1, m) = img_1 \times m, \qquad (19)$$

and m is an applied matrix.

To flip a 2D image vertically, we have to reverse the order of the pixels in each column of the image. This can be done by applying a transformation matrix to the coordinates of each pixel. The transformation matrix for vertical flipping is

$$Ver = \begin{bmatrix} 1 & 0 & 0 \\ 0 & -1 & h \\ 0 & 0 & 1 \end{bmatrix}, \qquad (20)$$

where h is the image height. This matrix will multiply each pixel coordinate (y) by -1 and then add h to the result, effectively moving the pixel to the opposite side of the image. The x coordinate will remain unchanged. For example, if the image has a height of 10 pixels and we want to flip the pixel at $(3, 4)$, we get

$$\begin{bmatrix} 1 & 0 & 0 \\ 0 & -1 & 10 \\ 0 & 0 & 1 \end{bmatrix} \begin{bmatrix} 3 \\ 4 \\ 1 \end{bmatrix} \begin{bmatrix} 3 + 0 \\ -4 + 10 \\ 1 + 0 \end{bmatrix} \begin{bmatrix} 3 \\ 6 \\ 1 \end{bmatrix}. \qquad (21)$$

Therefore the pixel at $(3, 4)$ will be moved to $(3, 6)$. In this way, we can flip the entire image vertically,

$$flip\_vertical(img_1) = apply(img_1, Ver). \qquad (22)$$

In our paper, we have used a random float generator named the Mersenne Twister algorithm. It is a pseudorandom number generator developed by Makoto Matsumoto and Takuji Nishimura in 1997. It is based on a matrix linear recurrence over a finite binary field. It can produce high-quality pseudorandom numbers that pass many statistical tests of randomness.

A pseudocode for the Mersenne Twister algorithm is presented as Algorithm 1. Here, $\oplus$ is the bitwise XOR operation, $\gg$ and $\ll$ are the bitwise right and left shift operations, respectively, and $\wedge$ is the bitwise AND operation. The constants N, M, R, A, U, D, S, B, T, C, and L are chosen based on the word size (32 or 64 bits) and the Mersenne prime. The masks UPPER_MASK and LOWER_MASK are derived from R. To generate a random float in the range $[0, 1)$, we can divide the output of *ExtractNumber* by the maximum possible value, which is either $2^{32} - 1$ or $2^{64} - 1$, depending on the word size. Alternatively, we can use the output bits directly as the binary representation of a floating-point number, as long as we avoid generating zero or one.

In such way a function $random\_float(a, b)$ can be written as follows:

$$random\_float(a, b)$$
$$= \frac{ExactNumber()}{(2^{32} - 1)} \times (a - b) + a . \qquad (23)$$

4. Proposed solution

The manual way of classification organs based on microscope imagery can be difficult and time consuming. To deal with this issue, this paper presents a lightweight deep learning solution allowing for accurate and quick classification of tissues origin. Presented solution can be found in Fig. 4. The architecture is based on a convolutional neural network architecture. To improve the data flow and reduce the negative impact of a large number of layers on signal decay, the architecture includes usage of residual connections, which strengthens the signal adding extra information for the later layers. Additionally, batch and layer normalization layers are added in empirically set positions in order to normalize the signal. Such combination allows for addition of more neuron layers, which improves the final understanding of the problem by the network. As an activation function, the rectified linear-unit (ReLU) has been chosen as it is computationally lightweight and gives enough complexity for achieving high accuracy. Its defining equation is

$$y' = \max(0, y). \qquad (24)$$

For the last layer, we have used the softmax activation function

$$\sigma(z_i) = \frac{e^{z_i}}{\sum_{j=1}^{K} e^{z_j}}, \quad i = 1, 2, \dots, K. \qquad (25)$$

Algorithm 1. Mersenne Twister algorithm for random float generation.

Initialize an array $MT[0 \dots N - 1]$ with a seed
$index \leftarrow N$
EXTRACT NUMBER
if $index \geq N$ **then**
   TWIST
end if
$y \leftarrow MT[index]$
$y \leftarrow y \oplus ((y \gg U) \wedge D)$
$y \leftarrow y \oplus ((y \ll S) \wedge B)$
$y \leftarrow y \oplus ((y \ll T) \wedge C)$
$y \leftarrow y \oplus (y \gg L)$
$index \leftarrow index + 1$
RETURN y
TWIST
for i from 0 to $N - 1$ **do**
   $x \leftarrow (MT[i] \wedge UPPER\_MASK) + (MT[(i + 1) \bmod N] \wedge LOWER\_MASK)$
   $x_A \leftarrow x \gg 1$
   if x is odd **then**
      $x_A \leftarrow x_A \oplus A$
   end if
   $MT[i] \leftarrow MT[(i + M) \bmod N] \oplus x_A$
end for
$index \leftarrow 0$

To keep the neural network small enough for quick training and evaluation the number of residual blocks has been kept at three, each one ending with a MaxPooling layer. The number of convolutional layers per residual block has been also reduced in comparison with popular models like ResNet50 or DenseNet. Such a modification allowed for better accuracy achieved in a smaller number of epochs on the given dataset as there was a smaller number of weights to optimize. For the training a modified NAdam algorithm was introduced that includes vector clamping in order to improve training stability.

Algorithm 2. Image augmentation algorithm.

Require: $img_1, lab_1, img\_res, \psi$
1: $img_1 := 255 - img_1$
2: $img_1 := resize(img_1, img\_res, img\_res)$ (2)
3: $output\_list := []$
4: **if** $\psi > 1$ **then**
5:    $i := 0$
6:    **for** $i < \psi$ **do**
7:       $img_2 := img_1$
8:       STAGE I - Image rotation
9:       $\beta := random\_float(0, 1)$
10:      **if** $\beta > 0.3$ **then**
11:        $\alpha := random\_float(-30, 30)$ (23)
12:        $img_2 := rotate(img_2, \alpha)$ (5)
13:      **end if**
14:      STAGE II - Color Jitter
15:      $\alpha_1 := random\_float(0.8, 1.2)$
16:      $\alpha_2 := random\_float(0.8, 1.2)$
17:      $\alpha_3 := random\_float(0.8, 1.2)$
18:      $\alpha_4 := random\_float(-0.1, 0.1)$
19:      $img_2 := change\_saturation(img_2, \alpha_1)$ (10)
20:      $img_2 := change\_brightness(img_2, \alpha_2)$ (11)
21:      $img_2 := change\_contrast(img_2, \alpha_3)$ (13)
22:      $img_2 := change\_hue(img_2, \alpha_4)$ (15)
23:      $\beta := random\_float(0, 1)$
24:      STAGE III - Image flipping
25:      **if** $\beta > 0.5$ **then**
26:        $img_2 := flip\_horizontal(img_2)$ (18)
27:      **end if**
28:      $\beta := random\_float(0, 1)$
29:      **if** $\beta > 0.5$ **then**
30:        $img_2 := flip\_vertical(img_2)$ (22)
31:      **end if**
32:      $img_2 := img_2/255.0$ {Normalization}
33:      $output\_list.append(img_2, lab_1)$
34:    **end for**
35: **end if**
36: $img_1 := img_1/255.0$ {Normalization}
37: $output\_list.append(img_1, lab_1)$
38: **return** $output\_list$ {Returns output batch of augmented images}

4.1. Backpropagation. Backpropagation is a method of training artificial neural networks by adjusting the weights of the connections in the network based on the error between the desired output and the actual output.

The algorithm can be written as follows.

Input data:

   $X =$ input data matrix of size $n \times d$,

   $Y =$ output data matrix of size $n \times k$,

   $f =$ activation function (e.g., sigmoid, ReLU, etc.),

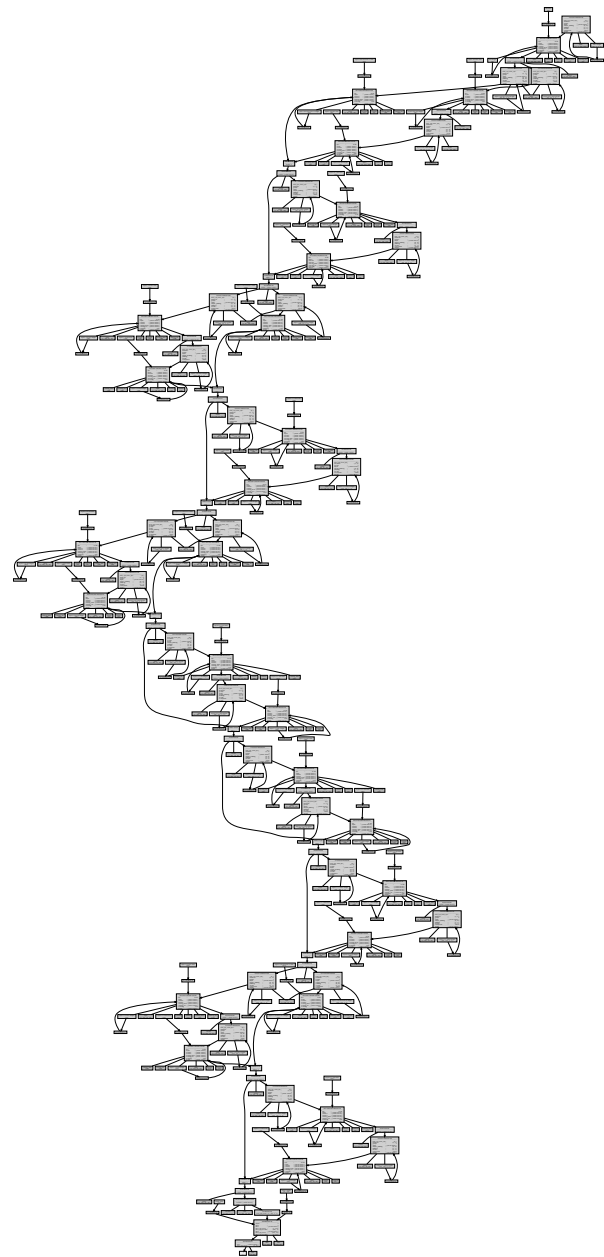 $L =$ loss function (e.g., mean squared error, etc.),

Fig. 4. Proposed deep neural network architecture.

$W^{(1)}, \ldots, W^{(m)} =$ weight matrices
$\qquad\qquad$ of consecutive layers,

$b^{(1)}, \ldots, b^{(m)} =$ bias vectors
$\qquad\qquad$ of consecutive layers.

Forward pass:

$$Z^{(1)} = XW^{(1)} + b^{(1)},$$
$$A^{(1)} = f(Z^{(1)}),$$
$$Z^{(2)} = A^{(1)}W^{(2)} + b^{(2)},$$
$$A^{(2)} = f(Z^{(2)}),$$
$$\vdots$$
$$Z^{(m)} = A^{(m-1)}W^{(m)} + b^{(m)},$$
$$A^{(m)} = f(Z^{(m)}),$$
$$\hat{Y} = A^{(m)}.$$

Backward pass:

$$
\begin{aligned}
E &= L(Y, \hat{Y}), \\
dZ^{(m)} &= f'(Z^{(m)}) \times E, \\
dW^{(m)} &= A^{(m-1)^T} dZ^{(m)}, \\
db^{(m)} &= dZ^{(m)}, \\
dA^{(m-1)} &= dZ^{(m)} W^{(m)^T}, \\
dZ^{(m-1)} &= f'(Z^{(m-1)}) \times dA^{(m-1)}, \\
dW^{(m-1)} &= A^{(m-2)^T} dZ^{(m-1)}, \\
db^{(m-1)} &= dZ^{(m-1)}, \\
dA^{(m-2)} &= dZ^{(m-1)} W^{(m-1)^T}, \\
&\vdots \\
dZ^{(1)} &= f'(Z^{(1)}) \times dA^{(1)}, \\
dW^{(1)} &= X^T dZ^{(1)}, \\
db^{(1)} &= dZ^{(1)}.
\end{aligned}
\qquad (26)
$$

Update weights and biases:

$$W^{(i)} := W^{(i)} - lr \times dW^{(i)},$$
$$b^{(i)} := b^{(i)} - lr \times db^{(i)},$$
$$\text{for } i = 1, 2, \ldots, m,$$

where lr is the learning rate, a hyper-parameter that controls how much the weights and biases are updated in each iteration. The algorithm can be repeated until the loss function reaches a minimum or a desired accuracy is achieved.

4.2. NAdam training algorithm. In order to improve the model's performance in terms of final accuracy, as well as the training times, we have used a slightly customized NAdam training algorithm on top of the classical backpropagation with parameters with a learning rate of 0.0001 and logarithmic decay, $\beta_1 = 0.925$, $\beta_2 = 0.998$. The NAdam formula can be described as follows:

$$z_t = \beta_1 z_{t-1} + (1 - \beta_1) p_t, \qquad (27)$$

$$k_t = \beta_2 k_{t-1} + (1 - \beta_2) p_t^2, \qquad (28)$$

where p is the current gradient of an error function and β_1 and β_2 are constant hyper-parameters. The values of z_t and k_t are used for calculation of the correlations marked as $\hat{z}_t$ and $\hat{k}_t$ according to

$$\hat{z}_t = (1 - \beta_1) p_t + \beta_{1_{t+1}} z_t, \qquad (29)$$

$$\hat{k}_t = \frac{k_t}{1 - \beta_2^t}. \qquad (30)$$

Finally, using the previously calculated correlations, the final formula can be defined as

$$w_t = w_{t-1} - LR \frac{\hat{z}_t}{\sqrt{\beta_{2_t}} + \epsilon}, \qquad (31)$$

where ϵ is a small constant, w are model weights and LR is the learning rate.

In the presented modification, however, the weights' update equation has been changed to include clamping for the weights' change vector in order to reduce the overflow and improve the network stability. The modified equation is:

$$w_t = w_{t-1} - LR \times \text{clamp}\Big(\frac{\hat{z}_t}{\sqrt{\beta_{2_t}} + \epsilon}, -\phi, \phi\Big), \quad (32)$$

where ϕ has been empirically set to be initially 1.586 and with a decay connected to the learning rate.

The applied loss function used in the presented training was the mean squared logarithmic error

$$L(y, \hat{y}) = \frac{1}{N} \sum_{i=0}^{N} (\log(y_i + 1) - \log(\hat{y}_i + 1))^2. \quad (33)$$

Due to its nature, it gave the best results for the given problem. The training process is also described as Algorithm 3.

4.3. Used hardware and performance. In this paper all computations including training have been performed on a 2023 Apple MacBook Pro with the following configuration:

- CPU: Apple M2 Max 12c,

- GPU: Apple M2 Max 38c,

- RAM: 96 GB.

Algorithm 3. NAdam training process.

1: Random weights generation,
2: **while** *global error value ε < error_value* **do**
3:   Shuffle the training set TS,
4:   **for** each mini-batch inside TS **do**
5:     Step = Step + 1,
6:     Calculate gradient vector p on the mini-batch,
7:     Update vector z using (27),
8:     Update vector k using (28),
9:     Rescale vector $\hat{z}$ using (29),
10:     Rescale vector $\hat{k}$ using (30),
11:     Update weights $\hat{w}_t$ using (32).
12:   **end for**
13:   Compute *global error ε*,
14: **end while**

Table 1. Comparison of different batch sizes and training times per epoch.

Batch size	Time per epoch
8	29 s/epoch
16	26 s/epoch
32	27 s/epoch

Table 2. Comparison between different batch sizes and inference time per batch.

Batch size	Time per batch
2	1 s/batch
4	2 s/batch
8	4 s/batch
16	6 s/batch
32	11 s/batch
64	22 s/batch

The final training took around 35 minutes and yielded a validation accuracy of 98.34%. Table 1 presents training times for different batch sizes. As can be seen, the best performance can be found with a batch size of 16, which was used in the final training. In Table 2 we can see inference times for different numbers of images. Here we can see a trend where more images per batch to some point are faster to process due to memory bandwidth. There also can be seen that on used hardware the analysis is very quick allowing the doctor to perform many checks per session.

5. Results

After around 35 minutes of training the proposed solution reached its peak validation accuracy of 98.34%, F_1 of 0.9847, 0.9878 precision and 0.9852 recall, using 85:15 split ratio for the training and validation sets. It is a very high score, especially considering that many of the images were contained in regions that were not characteristic
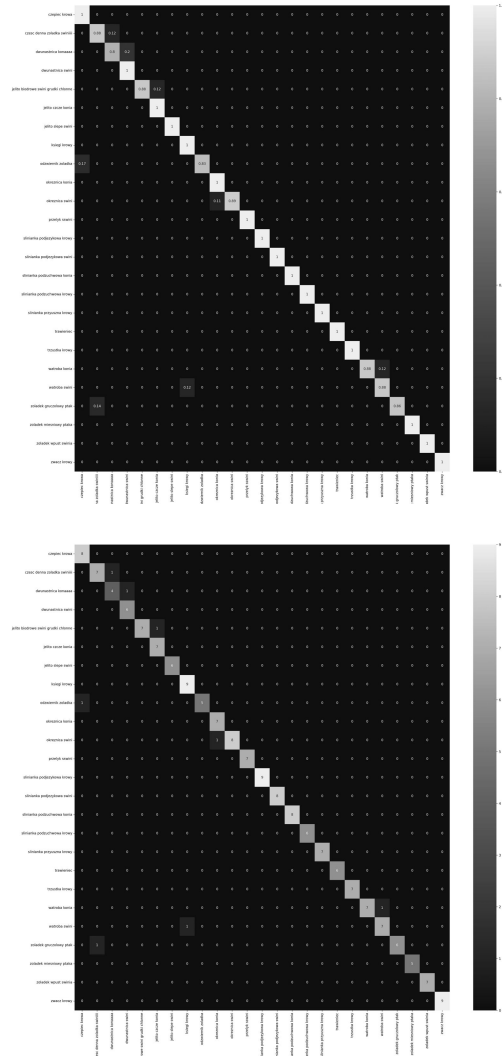

Fig. 5. Confusion matrix for network evaluation on validation data.

to the specific organ and also that there is no visible difference for a human specialist between the same organ from different species. The proposed solution however was able to differentiate them correctly in mostcases. The confusion matrices are shown in Fig. 5. As can be seen, the solution has a strong understanding of the given problem and mistakes are very uncommon.

5.1. Comparison with the state of the art. To validate our results, a comparison between the presented model and other similar state-of-the-art papers has been made, cf. Table 3. As we can see, the direct comparison is not possible as the majority of models are based on much fewer abstract classes and only from one species–Human; however it is still important to compare the accuracy of such models to have a better understanding of the quality
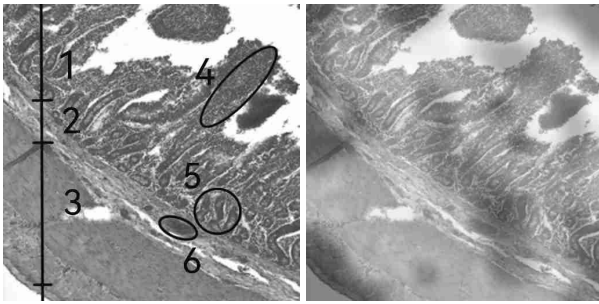
Fig. 6. Ileum of a pig with mucous membrane (1), submucous membrane (2), muscular membrane (3), intestinal villi (4), intestinal glands (5) and lymphatic follicle (6) (H+E). Objective magnification: 10×.
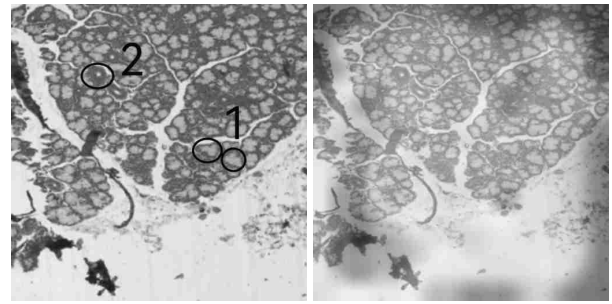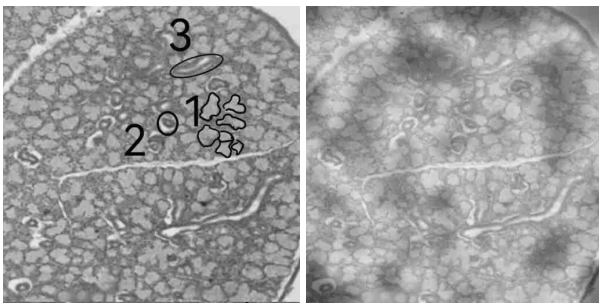

Fig. 7. Sublingual salivary gland of a pig with secretory sections (1), intercalated duct (2) and and striated duct (3) (H+E). Objective magnification: 10×.

Fig. 8. Liver of a pig with interlobular connective tissue (1), liver lobule (2), portal area with liver triad (3) (H+E). Objective magnification: 10×.

Fig. 9. Sublingual salivary gland of a cow with secretory sections (1), intercalated and striated ducts (2) (H+E). Objective magnification: 10×.
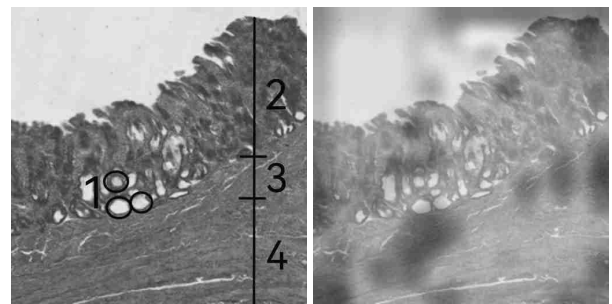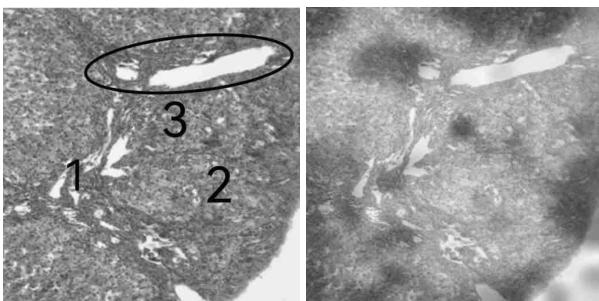

Fig. 10. Gizzard with simple tubular glands (1), mucous membrane (2), submucous membrane (3), muscular membrane (4) (H+E). Objective magnification: 10×.
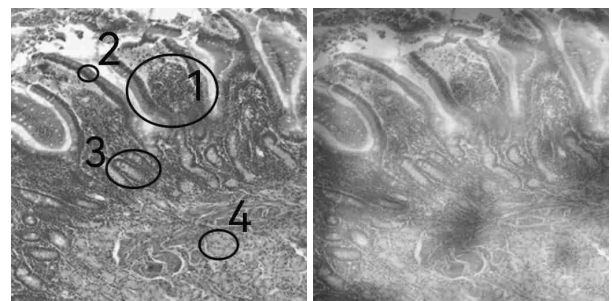

Fig. 11. Duodenum of a pig with intestinal villi (1), simple columnar epithelium with goblet cells (2), intestinal glands (3), duodenal glands (4) (H+E). Objective magnification: 40×.

of our work. One of the best architectures from our table is made by Khorshed *et al.* (2020). Their accuracy is a little higher than our model, but they had fewer classes and all images came from human patients, which creates a simpler problem than multi-species classification with a large number of variables. Another interesting paper is that by Ker *et al.* (2019), where tissue tumor detection was investigated using Google's inception model. Although they used a transfer learning method for an initial weight setup and a known, high performance deep learning model, their accuracy was smaller than ours, reaching 96%. A similar solution was also proposed by Zahia *et al.*

(2018), where a custom convolutional neural network for tissue pressure injuries was presented. Their model reached a peak accuracy of 92.01% on the employed dataset, which is much smaller than in our solution. Another work by Fragoso-Garcia *et al.* (2023) achieved a good accuracy of 95%, however their number of abstract classes was smaller. Finally, Vang *et al.* (2018) presented an interesting model for tissue analysis using a convolutional neural network and reached a validation accuracy of 87.5%.

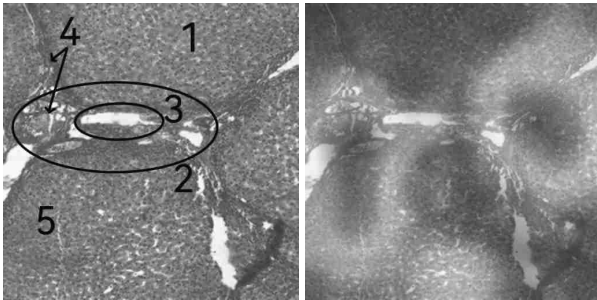To test the proposed model more fairly in comparison

Fig. 12. Liver of a pig with hepatocytes (1), portal area with liver triad (2), venous vessel (3), interlobular connective tissue (4), liver lobule (5) (H+E). Objective magnification: 10x.
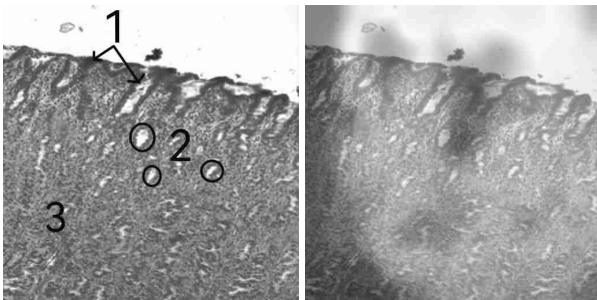

Fig. 13. Mucous membrane of the stomach (fundus) of a pig with simple columnar epithelium (1), gastric glands (2), lamina propria of mucosa (3) (H+E). Objective magnification: 40×.
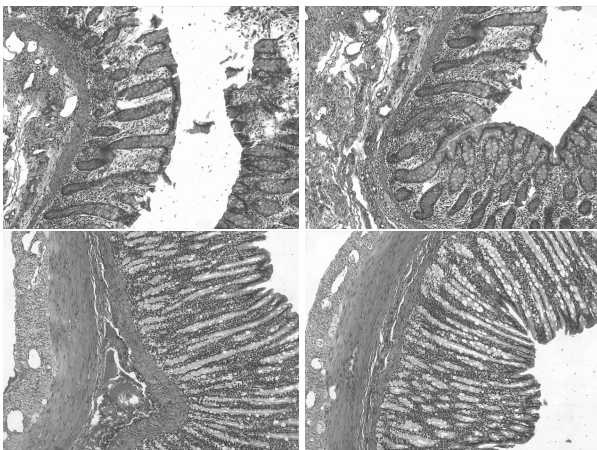

Fig. 14. Two upper images presents colon of a horse and the lower two images presents the colon of a pig. As we can see, there are very little visual differences between those two species, making it difficult to correctly differentiate them. Our proposed neural network, however, is able to correctly classify them. Objective magnification: 40×.

with other popular models, we trained models ResNet50 and Vit16 on the presented dataset. After 35 minutes of training, ResNet50 achieved an accuracy of 97.24% which is worse by a little amount; however, Vit16 could not achieve good results on these data having only an accuracy of 13.81%. All models were trained with a batch size of 16, the same image size and augmentation. More information can be found in Table 3. As can be seen, our model has similar training times and memory usage per epoch in comparison with ResNet50; however, even with that disadvantage, during the same training time it converges much faster creating a better performing model for this usage. Vit16, however, has much higher memory usage and performs much slower in terms of the training time per epoch. On this dataset it also achieves the worse accuracy.

In conclusion, although the current state-of-the-art papers present some interesting solution for tissue analysis, the vast majority of them has a small, specialized field in which they work (mostly cancer or injuries detection) with a low number of abstract classes and also work only on one species, mostly human. Such works are valid for medicine; however, our method is a new and novel addition to veterinary medicine, which is not yet common. What is more, our results are outstanding and can compete not only in veterinary medicine but also in human one in terms of performance and accuracy.

5.2. Comparison between human specialists and the proposed solution. In order to classify the sample in Fig. 6, human specialists focus mostly on a region with intestinal villi marked as 4, intestinal glands (5) and lymphatic follicles (6), which are characteristic to this organ. The proposed solution in this case focuses its attention on similar regions. In both the samples, showed in Figs. 7 and 9, human specialists classify the origin of the sample by looking at the ratios of the listed elements, as depending on the species those are different. By analyzing the network's attention map it can be concluded that in these examples the proposed solution has a similar approach as well. In Figs. 8 and 12 the traditional method focuses on the listed structures and the presence of hepatocytes, which are characteristic to the liver. In these examples, however, the proposed solution, although focusing on some of the marked regions, adds its own places of attention in order to correctly differentiate the origin of samples. In Fig. 10 specialists focus on the overall shape of the structure with the emphasis on simple tubular glands (1). The proposed solution, however, focuses its attention mostly on the muscular membrane (4) and the submucous membrane (3). In the example, paid 11 human specialists focus mostly on all listed elements with special attention paid to duodenal glands (4), which are characteristic to duodenum. In this case the proposed solution has a similar approach as well. Finally in Fig. 13

Table 3. Comparison between the presented model and other popular models in terms of training times and memory usage.

Model	Memory	Time per epoch
Our	4.06 GB	26 s/epoch
ResNet50	3.4 GB	25 s/epoch
Vit16	6.22 GB	63 s/epoch

Table 4. Comparison between the presented model and other similar papers.

Model	Year	Accuracy
Ours (Animals)	2023	98.34%
Ker *et al.* (2019) (Human)	2019	96.00%
Zahia *et al.* (2018) (Human)	2018	92.01%
Khorshed *et al.* (2020) (Human)	2020	98.90%
Vang *et al.* (2018) (Human)	2018	87.50%
Fragoso-Garcia *et al.* (2023)	2023	95.00%
ResNet50 (Animals)	2024	97.24%
Vit16 (Animals)	2024	13.81%

all listed elements are necessary for classification but the importance is mostly set to gastric glands (2), which are characteristic to the stomach. The proposed solution has also similar areas of focus.

6. Conclusion

The final presented network reached a high accuracy on the validation data, especially taking account of the high similarity of the tissues between different organs of various species making it sometimes impossible to correctly classify even for a trained professional. Because of that, the proposed deep learning solution can be treated as a successful attempt to solve the presented problem. This paper also presents a well-functioning pipeline of data augmentation without losing any important data and providing misleading samples. In such a way, the final network was able to reach a much higher accuracy than on the original dataset. What is also important, this work ensures the quality of the dataset by creating a custom one with the focus on the balance between classes, high quality of images and photographing regions ambiguous for humans, which allowed a deep learning solution to work also on such data. Another fact is that there were no public datasets containing such a variety of classes for animal tissue origin detection, which was the main focus of the presented work. Because of this, the paper is one of the first such works in the public domain. The presented model can also be a useful addition to the education sector as a helper for students during learning differences between organs and tissues, especially when working with freshly collected samples without prior knowledge about the exact origin. In the current state of the work, the accuracy of the presented architecture is high and provides good results even in very difficult scenarios; however, at this moment there is a limited number of abstract classes, which could not be enough for a full diagnosis. The model is also lightweight. However, although it can run even on low performance computers, more work could be done to make it even less resource intensive to allow for more mobile inference.

7. Future possibilities

In the future, there is a possibility to create an extended dataset by photographing more samples per available classes and also by adding new categories. In such a way, the network would be even more useful and have a better understanding of the analyzed problem. There is also a possibility to improve the data augmentation pipeline and fine-tune the deep learning architecture to improve the final accuracy even more. Another possibility is to create a new dataset focused on different regions of the body or to include a semantic segmentation architecture for adding more information for the user about the evaluated tissue.

Another important possibility is to use the presented dataset as a template for a neural network model able to detect abnormalities in photographed tissues based on the healthy data collected in this paper. Such work can be very helpful in pathology classification and detection. However, without the knowledge of a healthy tissue image it will not work properly making the presented work an important step in finding a solution for such a problem.

Acknowledgment

References

Abayomi-Alli, O.O., Damaševičius, R., Wieczorek, M. and Woźniak, M. (2020). Data augmentation using principal component resampling for image recognition by deep learning, *Artificial Intelligence and Soft Computing: 19th International Conference, ICAISC 2020, Zakopane, Poland*, pp. 39–48.

Al-Juboory, R.W., Dauod, H.A. and Al-arajy, A.S. (2017). Comparative anatomical and histological study of the stomach in two IRAQI BIRDS (columba palumbus and tyto alba), *IBN AL-Haitham Journal For Pure and Applied Science* **29**(2): 1–12.

Amorim, I., Taulescu, M., Day, M., Catoi, C., Reis, C., Carneiro, F. and Gärtner, F. (2016). Canine gastric pathology: A review, *Journal of Comparative Pathology* **154**(1): 9–37.

Angelou, V., Fiska, A., Tsingotjidou, A., Patsikas, M. and Papazoglou, L.G. (2023). Surgical anatomy of the gastrointestinal tract in cats, *Animals* **13**(16): 2670.

Bacha Jr, W.J. and Bacha, L.M. (2012). *Color Atlas of Veterinary Histology*, Wiley, Hoboken.

Badawi, H., A Abd El-Rahman, Y., Salem, A. and Mohamed, A. (1998). Comparative morphological studies on the intestinal glands of the colon and rectum of some domestic animals, *Assiut Veterinary Medical Journal* **39**(77): 36–53.

Banzato, T., Gelain, M. E., Aresu, L., Centelleghe, C., Benali, S.L. and Zotti, A. (2015). Quantitative analysis of ultrasonographic images and cytology in relation to histopathology of canine and feline liver: An ex-vivo study, *Research in Veterinary Science* **103**: 164–169.

Basran, P. (2024). New horizons: Artificial intelligence in veterinary medicine, *An interview*, Cornell University, Ithaca, https://www.vet.cornell.edu/news/20 230106/new-horizons-artificial-intelli gence-veterinary-medicine.

Bazira, P.J. (2023). Anatomy of the oesophagus, *Surgery (Oxford)* **41**(11): 691–697.

Bodes, F.J.S. and Martínez, F.J.P. (2023). *Aughey and Frye's Comparative Veterinary Histology with Clinical Correlates*, CRC Press, Boca Raton.

Botlagunta, S. and Kedari, S. (2023). Histoarchitectural and histochemical studies on the oesophagus of local dog, *The Pharma Innovation Journal* **12**(2): 1560–1565.

Carubbi, F., Alunno, A., Gerli, R. and Giacomelli, R. (2018). Histopathology of salivary glands, *Reumatismo—The Italian Journal of Rheumatology* **70**(3): 146–154.

Catroxo, M., Lima, M. and Cappellaro, C. (1997). Histological aspects of the stomach (proventriculus and gizzard) of the red-capped cardinal (paroaria gularis gularis, linnaeus, 1766), *Revista Chilena de Anatomía* **15**(1): 19–27.

Chivers, D.J. and Hladik, C.M. (1980). Morphology of the gastrointestinal tract in primates: Comparisons with other mammals in relation to diet, *Journal of Morphology* **166**(3): 337–386.

Chungath, J.J. (1981). *Anatomy and Histology of Ruminant Stomach of Goat*, PhD thesis, College of Veterinary and Animal Sciences, Mannuthy.

Dawood, M.S., Abood, D.A. and Hameza, A.Y. (2022). The histological and histochemical features of the esophagus in local breed dogs (canis familiaris), *Iraqi Journal of Veterinary Sciences* **36**(4): 1069–1074.

Doyama, H., Nakanishi, H. and Yao, K. (2021). Image-enhanced endoscopy and its corresponding histopathology in the stomach, *Gut and Liver* **15**(3): 329.

Eberlova, L., Maleckova, A., Mik, P., Tonar, Z., Jirik, M., Mirka, H., Palek, R., Leupen, S. and Liska, V. (2020). Porcine liver anatomy applied to biomedicine, *Journal of Surgical Research* **250**: 70–79.

Ezanno, P., Picault, S., Beaunée, G., Bailly, X., Muñoz, F., Duboz, R., Monod, H. and Guégan, J.-F. (2021). Research perspectives on animal health in the era of artificial intelligence, *Veterinary Research* **52**: 1–15.

Fragoso-Garcia, M., Wilm, F., Bertram, C.A., Merz, S., Schmidt, A., Donovan, T., Fuchs-Baumgartinger, A., Bartel, A., Marzahl, C., Diehl, L., Puget, C., Maier, A., Aubreville, M., Breininger, K. and Klopfleisch, R. (2023). Automated diagnosis of 7 canine skin tumors using machine learning on H&E-stained whole slide images, *Veterinary Pathology* **60**(6): 865–875.

Friedland, G.W., Kohatsu, S. and Lewin, K. (1971). Comparative anatomy of feline and canine gastric sling fibers: Analogy to human anatomy, *American Journal of Digestive Diseases* **16**: 495–507.

Ghoshal, N. and Bal, H. (1989). Comparative morphology of the stomach of some laboratory mammals, *Laboratory Animals* **23**(1): 21–29.

Hewetson, M. and Tallon, R. (2021). Equine squamous gastric disease: Prevalence, impact and management, *Veterinary Medicine: Research and Reports* **21**(2021): 381–399.

Hogben, C.A.M., Kent, T.H., Woodward, P.A. and Sill, A. (1974). Quantitative histology of the gastric mucosa: Man, dog, cat, guinea pig, and frog, *Gastroenterology* **67**(6): 1143–1154.

Hostetter, J.M. and Uzal, F.A. (2022). Gastrointestinal biopsy in the horse: Overview of collection, interpretation, and applications, *Journal of Veterinary Diagnostic Investigation* **34**(3): 376–388.

Hristov, H. (2020). Avian stomach anatomy—A mini review, *Bulgarian Journal of Veterinary Medicine* **24**(4): 461–468.

Jones, K.R., John, R.E. and Sundaram, V. (2022). Morpho-histological studies of the gastrointestinal tract of the orange-rumped agouti (dasyprocta leporina linnaeus, 1758), with special reference to morphometry and histometry, *Animals* **12**(19): 2493.

Kararli, T.T. (1995). Comparison of the gastrointestinal anatomy, physiology, and biochemistry of humans and commonly used laboratory animals, *Biopharmaceutics & Drug Disposition* **16**(5): 351–380.

Karlupia, N., Mahajan, P., Abrol, P. and Lehana, P.K. (2023). A genetic algorithm based optimized convolutional neural network for face recognition, *International Journal of Applied Mathematics and Computer Science* **33**(1): 21–31, DOI: 10.34768/amcs-2023-0002.

Ker, J., Bai, Y., Lee, H.Y., Rao, J. and Wang, L. (2019). Automated brain histology classification using machine learning, *Journal of Clinical Neuroscience* **66**: 239–245.

Khorshed, T., Moustafa, M.N. and Rafea, A. (2020). Deep learning for multi-tissue cancer classification of gene expressions (GeneXNet), *IEEE Access* **8**: 90615–90629.

Kotzé, S.H., Van Der Merwe, E.L., Bennett, N.C. and O'Riain, M.J. (2010). The comparative anatomy of the abdominal gastrointestinal tract of six species of African mole-rats (rodentia, bathyergidae), *Journal of Morphology* **271**(1): 50–60.

Kuryszko, J., Madej, J.P. and Kapuśniak, V. (2019). *Guidebook to Animal History*, Wroclaw University of Environmental and Life Science, Wroclaw, (in Polish).

Lechner-Doll, M., Von Engelhardt, W., Abbas, H., Mousa, L., Luciano, L. and Reale, E. (1995). Particularities in forestomach anatomy, physiology and biochemistry of camelids compared to ruminants, *in* J.-L. Tisserand (Ed.), *Elevage et alimentation du dromadaire*, CIHEAM, Zaragoza, pp. 19–32.

Lidbury, J., Rodrigues Hoffmann, A., Ivanek, R., Cullen, J., Porter, B., Oliveira, F., Van Winkle, T., Grinwis, G., Sucholdolski, J. and Steiner, J.M. (2017). Interobserver agreement using histological scoring of the canine liver, *Journal of Veterinary Internal Medicine* **31**(3): 778–783.

Lingeman, C.H. and Garner, F. (1972). Comparative study of intestinal adenocarcinomas of animals and man, *Journal of the National Cancer Institute* **48**(2): 325–346.

Longnecker, D.S. and Thompson, E.D. (2023). Anatomy, histology, and fine structure of the pancreas, *in* H.G. Beger *et al.* (Eds), *The Pancreas: An Integrated Textbook of Basic Science, Medicine, and Surgery* Wiley-Blackwell, Hoboken, pp. 9–22.

Mahadevan, V. (2020). Anatomy of the oesophagus, *Surgery (Oxford)* **38**(11): 677–682.

Markovits, J.E., Betton, G.R., McMartin, D.N. and Turner, O.C. (2013). Gastrointestinal tract, *in* P.S. Sahota *et al.* (Eds), *Toxicological Pathology Nonclinical Safety Assessment,* CRC Press, Boca Raton, pp. 257–312.

McQuilken, S.A. (2021). The mouth, stomach and intestines, *Anaesthesia & Intensive Care Medicine* **22**(5): 330–335.

Newman, S., Steiner, J., Woosley, K., Williams, D. and Barton, L. (2006). Histologic assessment and grading of the exocrine pancreas in the dog, *Journal of Veterinary Diagnostic Investigation* **18**(1): 115–118.

Oza, P., Sharma, P., Patel, S., Adedoyin, F. and Bruno, A. (2022). Image augmentation techniques for mammogram analysis, *Journal of Imaging* **8**(5): 141.

Porcheri, C. and Mitsiadis, T.A. (2019). Physiology, pathology and regeneration of salivary glands, *Cells* **8**(9): 976.

Rak, E., Szczur, A., Bazan, J.G. and Bazan-Socha, S. (2023). Assessment measures of an ensemble classifier based on the distributivity equation to predict the presence of severe coronary artery disease, *International Journal of Applied Mathematics and Computer Science* **33**(3): 361–377, DOI: 10.34768/amcs-2023-0026.

Rakha, E.A., Toss, M., Shiino, S., Gamble, P., Jaroensri, R., Mermel, C.H. and Chen, P.-H. C. (2021). Current and future applications of artificial intelligence in pathology: A clinical perspective, *Journal of Clinical Pathology* **74**(7): 409–414.

Sellers, A. and Stevens, C. (1966). Motor functions of the ruminant forestomach, *Physiological Reviews* **46**(4): 634–661.

Sheahan, D.G. and Jervis, H.R. (1976). Comparative histochemistry of gastrointestinal mucosubstances, *American Journal of Anatomy* **146**(2): 103–131.

Shiina, T., Shimizu, Y., Izumi, N., Suzuki, Y., Asano, M., Atoji, Y., Nikami, H. and Takewaki, T. (2005). A comparative histological study on the distribution of striated and smooth muscles and glands in the esophagus of wild birds and mammals, *Journal of Veterinary Medical Science* **67**(1): 115–117.

Stieger-Vanegas, S.M. and McKenzie, E. (2021). Abdominal imaging in small ruminants: Liver, spleen, gastrointestinal tract, and lymph nodes, *Veterinary Clinics: Food Animal Practice* **37**(1): 55–74.

Suganuma, T., Katsuyama, T., Tsukahara, M., Tatematsu, M., Sakakura, Y. and Murata, F. (1981). Comparative histochemical study of alimentary tracts with special reference to the mucous neck cells of the stomach, *American Journal of Anatomy* **161**(2): 219–238.

Taki-El-Deen, F. (2017). Comparative microscopic study on the tongue, oesophagus and stomach of two different birds in Egypt, *The Egyptian Journal of Hospital Medicine* **67**(1): 359–365.

Tsuchitani, M., Sato, J. and Kokoshima, H. (2016). A comparison of the anatomical structure of the pancreas in experimental animals, *Journal of Toxicologic Pathology* **29**(3): 147–154.

Vang, Y.S., Chen, Z. and Xie, X. (2018). Deep learning framework for multi-class breast cancer histology image classification, *Image Analysis and Recognition: 15th International Conference, ICIAR 2018, Póvoa de Varzim, Portugal*, pp. 914–922.

Voutsinou, A., Papazoglou, L.G., Antonopoulos, I. and Rallis, T.S. (2018). Clinical topographical anatomy of the gastro-oesophageal junction in the cat, *Journal of Feline Medicine and Surgery* **20**(4): 308–311.

Watson, A.G. (1973). Structure of the canine oesophagus, *New Zealand Veterinary Journal* **21**(9): 195–200.

Wojtas, N., Wieczorek, M. and Bełkot, Z. (2023). Malaria detection using custom semantic segmentation neural network architecture, *Medycyna Weterynaryjna* **79**(8): 406–412.

Yang, L., Xie, T., Liu, M., Zhang, M., Qi, S. and Yang, J. (2023). Infrared small-target detection under a complex background based on a local gradient contrast method, *International Journal of Applied Mathematics and Computer Science* **33**(1): 33–43, DOI: 10.34768/amcs-2023-0003.

Zahariev, P., Sapundzhiev, E., Pupaki, D., Rashev, P., Palov, A. and Todorov, T. (2010). Morphological characteristics of the canine and feline stomach mucosa, *Anatomia, Histologia, Embryologia* **39**(6): 563–568.

Zahia, S., Sierra-Sosa, D., Garcia-Zapirain, B. and Elmaghraby, A. (2018). Tissue classification and segmentation of pressure injuries using convolutional neural networks, *Computer Methods and Programs in Biomedicine* **159**: 51–58.

Zhang, F., Yang, J., Nezami, N., Laage-Gaupp, F., Chapiro, J., De Lin, M. and Duncan, J. (2018). Liver tissue classification using an auto-context-based deep neural network with a multi-phase training framework, *Patch-Based Techniques in Medical Imaging: 4th International*

Workshop, Patch-MI 2018/MICCAI 2018, Granada, Spain, pp. 59–66.

Michał Wieczorek received his MS degree in computer science in 2024 from the Silesian University of Technology and is currently working on his PhD in artificial intelligence. He is a research assistant in the Faculty of Applied Mathematics, Silesian University of Technology in Poland. His main area of research interests include heuristics models for big data optimization and various deep learning techniques with the use of transformer models, convolutional architectures and recurrent neural networks for classification and regression. Currently his research especially focuses on analyzing and processing medical data using semantic segmentation and classification.

Natalia Wojtas received the title of a veterinary medicine doctor in 2024 from the University of Life Sciences in Lublin. She has been working as a researcher since early 2020, with special focus on fecal transplantation, infectious diseases, with emphasis on zoonotic diseases transmitted by wildlife animals and the brainsteam auditory evoked potentials (BAER) method. Her present interests include neurology with expansion of the current BAER methods for other animals and standardization of evaluation, pheasants parasitological and histological studies and epidemiological status of free living animals.

Roman Wituła received his PhD degree in 1997 at the University of Silesia in Katowice and his DSc degree in 2014 at the University of Lodz, both in mathematics. He is currently working as a researcher at the Silesian University of Technology. His main research area includes mathematical analysis, discrete mathematics and symbolic computation.

Aleksandra Krawczyk received the title of a veterinary medicine doctor in 2006 from the University of Life Sciences in Lublin. She has been working in the Department of Animal Anatomy and Histology of the University of Life Sciences in Lublin since 2009. She received a PhD degree in veterinary sciences from the Faculty of Veterinary Medicine, University of Life Sciences in Lublin, in 2015. She focuses on microscopic and morphometric analyses of histological slides of animal tissues. Her research interests especially include influence of different exogenous substances on central and peripheral nervous system. She is a co-author of 30 publications.

Karol Rycerz received the title of a veterinary medicine doctor in 2011 and a PhD in 2018, both from the University of Life Sciences in Lublin. He has been working in the Department of Animal Anatomy and Histology there since 2011. His research interests include influence of different substances on animal tissues with particular emphasis on the central nervous system. The research methods that he uses in his studies are microscopic and morphometric analyses of histological slides with standard and immunohistochemical staining.